Weld Pool Development during GTA and Laser Beam Welding of Type 304 Stainless Steel, Part II—Experimental Correlation

The predicted influence of surface active elements and temperature distribution on weld pool geometry are verified by experimentation

BY T. ZACHARIA, S. A. DAVID, J. M. VITEK AND T. DEBROY

ABSTRACT. In Part I of the paper, the results of the heat flow and the fluid flow analysis are presented. Here, in Part II of the paper, predictions of the computational model are verified by comparing the numerically predicted and experimentally observed fusion zone size and shape. Stationary gas tungsten arc and laser beam welds were made on Type 304 stainless steel for different times to provide a variety of solidification conditions such as cooling rate and temperature gradient. Calculated temperatures and cooling rates are correlated with the experimentally observed fusion zone structure. In addition, the effect of sulfur on GTA weld penetration was quantitatively evaluated by considering two heats of 304 stainless steel containing 90 and 240 ppm sulfur. Sulfur, as expected, increased the depth/width ratio by altering the surface tension gradient driven flow in the weld pool.

Following conventional welding, the weld metal solidified with a duplex $\gamma + \delta$ structure. The rapid solidification of the metal after laser beam welding resulted in a fully austenitic structure. A few of the laser beam welds that were made used argon shielding gas that was contaminated with oxygen. The effect of oxygen was to increase the depth, the width and the depth/width ratio considerably. The fusion zone structure showed a continuous oxide layer within the fusion zone that was later identified as Cr_2O_3. All of the effects can be better understood based on the modeling results in Part I.

Introduction

Welding is a complex process that involves many variables, any of which may have an important effect on the final solidification structure and properties of the welded joint. The intense heat source used in the welding process implies that very steep temperature gradients and high cooling rates can be generated in the weld zone, which can affect the ultimate properties of the weldment. The heat flow and the fluid flow in the weld pool can significantly influence the temperature gradients, the cooling rates and the solidification structure. In addition, the fluid flow and the convective heat transfer in the weld pool are known to control the penetration and shape of the weld pool. The depth of penetration achieved during welding can significantly influence the ultimate mechanical properties of the weldment. Often, the critical variable that controls variation in the pool geometry is the amount of surface active minor elements that are present in commercially available material. In iron-base alloys, sulfur and oxygen are the surface active elements most commonly present.

A surface tension gradient driven fluid flow model has been proposed by Heiple, *et al.* (Refs. 1–5), to explain the effect of surface active elements on gas tungsten arc (GTA) weld penetration. He proposed that the observed variation in weld penetration is due to an altered flow field in the weld pool caused by surface active elements. Additions of sulfur can cause changes in the spatial variation of surface tension, thereby altering the surface tension gradient driven flow. While the surface tension model has been supported by several theoretical and experimental investigations, there has been no coordinated attempt to correlate the findings of a numerical study with the experimental observations. Such comparisons can yield a quantitative understanding of the effect of fluid flow and heat transfer on the development of the weld pool.

KEY WORDS

Modeling of Welding
GTA Welding
Laser Beam Welding
304 Stainless Steel
Minor Elements
Weld Penetration
Surface Temperature
Cooling Rate
Rapid Solidification

The present investigation has been concerned with the heat transfer and fluid flow that occur during and after GTA and laser beam welding and their effects on the weld pool shape and the final solidification structure. Consequently, GTA and laser beam welds were made on the same material in order to evaluate the relative effect of the two processes on the observed shape of the weld and the solidification structure. In addition, the investigation focused on quantitatively evaluating the effect of sulfur on GTA weld penetration. Therefore, two heats of Type 304 stainless steel containing 90 and 240 ppm sulfur were utilized. The detailed information on the temperature distribution, the flow field and the cooling rates that a material experiences during welding is of considerable metallurgical importance. The theoretical investigation presented in Part I (Ref. 6) has dealt in detail with the fluid flow and heat transfer that occur during welding and the possible consequences on the weld pool shape, size and structure. Here in Part II, the predictions of the model are verified by comparing the predicted and experimentally observed weld pool shape and size. Finally, the calculated temperatures and cooling rates are correlated with the experimentally observed solidification structure.

Experimental Procedure

The materials used in this study consist of two heats of Type 304 stainless steel, and their compositions are given in Table

T. ZACHARIA, S. A. DAVID and J. M. VITEK are with the Metals and Ceramics Div., Oak Ridge National Laboratory, Oak Ridge, Tenn. T. DEBROY is with the Dept. of Materials Science and Engineering, Pennsylvania State University, University Park, Pa.

1. Stationary welds were made on 30 × 30 × 6-mm (1.2 × 1.2 × 0.24-in.) samples at the center of the specimen using conventional GTA and laser beam welding processes. The welding parameters used in this investigation are given in Table 2. The GTA welds were made with an Astro Arc, Astromatic E-300-P welding unit. The welding current and duration are entered through digital switches, enabling accurate programming. In addition, the arc current, the arc voltage and the cover gas flow were monitored using a CRC-Evans arc data monitor system to verify the welding parameters. The weld duration timer, Eagle Signal, is a digital system that bases its time reference on the frequency of the AC line. The timer starts once the arc is initiated and maintains the current at the selected current level. The specimens were held firmly by four bolts at the center of each of their lateral faces to provide a symmetrical current and magnetic field in the specimen. In addition, the fixture allowed convective and radiative heat transfer from all surfaces of the specimen.

Laser beam welds were made using a carbon dioxide laser, Coherent Model Everlase 525-1, capable of producing a maximum output of 575 W in the continuous wave mode. Welding was carried out inside a Plexiglass box under a controlled atmosphere using a 2.54-cm-diameter, 12.7-cm-focal-length Zn-Se lens with an antireflection coating.

The fusion zone size, shape and structure were examined by light microscopy. Particular care was taken to ensure that the samples were sectioned along the center of the weld. The specimens were prepared using standard procedures and then etched using HNO_3 and H_2O.

Results and Discussion

Macrostructure
GTA welds

First, the experimental results for the heat containing 90 ppm sulfur are presented in Fig. 1. Figure 1A shows the transverse section of the stationary GTA weld after 2 s. The macrograph shows a relatively shallow weld with a depth/width ratio of 0.27. The shape of the weld indicates that the weld pool experienced a radially outward flow during welding. The observed depth/width ratio is significantly lower than the values reported in the literature for Type 304 stainless steels with comparable sulfur content (Refs. 1–5). This discrepancy may be explained by the fact that the welds considered here are stationary welds. Under these conditions, the weld pool temperature is higher, resulting in a negative $\frac{d\gamma}{dT}$ over a larger area causing a predominantly outward flow. An outward flow would transport heat from the center to the periphery of the weld, which can explain the low depth/width ratio. The transverse section of the stationary GTA weld, after 5 s, is shown in Fig. 1B. There are no observable changes in the overall shape of the weld pool or the depth/width ratio with continued welding beyond 2 s. It must be pointed out that at temperatures close to the boiling point, the temperature coefficient of surface tension ($\frac{d\gamma}{dT}$) is not very sensitive to changes in temperature (Ref. 7). Any increase in the magnitude of $\frac{d\gamma}{dT}$ (due to increased surface temperature) may have been compensated by a reduction in the temperature gradients that exist on the weld pool surface (due to an increase in the width of the pool). This is consistent with the fluid flow calculations that showed that the maximum velocities at the weld pool surface and the weld pool depth to width ratio were the same after 2 and 5 s of welding (Ref. 6).

The results indicate that the development of the weld pool is essentially symmetrical about the axis of the electrode. However, at particular locations (far away from the weld pool surface) a lack of symmetry is observed, suggesting an unsteady flow field in the weld pool. Indeed, such flows are to be expected due to the presence of two strong and opposing forces, namely, the electromagnetic and the surface tension gradient forces. As a result, any local perturbation in the weld pool can cause the flow field to change dramatically, resulting in the observed lack of local symmetry. The results show inflections in the fusion zone interface (indicated by arrows) at locations where the electromagnetic force may have overcome the surface tension force, thereby, influencing convective heat transfer.

The second heat of Type 304 stainless steel considered in this investigation con-

Table 1—Alloy Composition (wt-%)

Element	Heat A	Heat B
Cr	18.27	18.28
Ni	8.73	9.46
Mn	1.71	1.88
C	0.025	0.031
Si	0.35	0.50
P	0.026	0.022
S	0.009	0.024
Mo	0.27	0.31
V	0.10	0.08
Cb	0.01	0.01
Ti	<0.01	<0.01
Co	0.14	0.15
Cu	0.19	0.15

Table 2—Welding Parameters (Stationary Welds)

GTA process	
Current	150 A
Voltage	14 V
Weld duration	2, 5 s
Shielding gas	20 ft^3/h argon
Laser beam process	
Power	500 W, continuous wave mode
Weld duration	2, 5 s
Shielding gas	20 ft^3/h argon

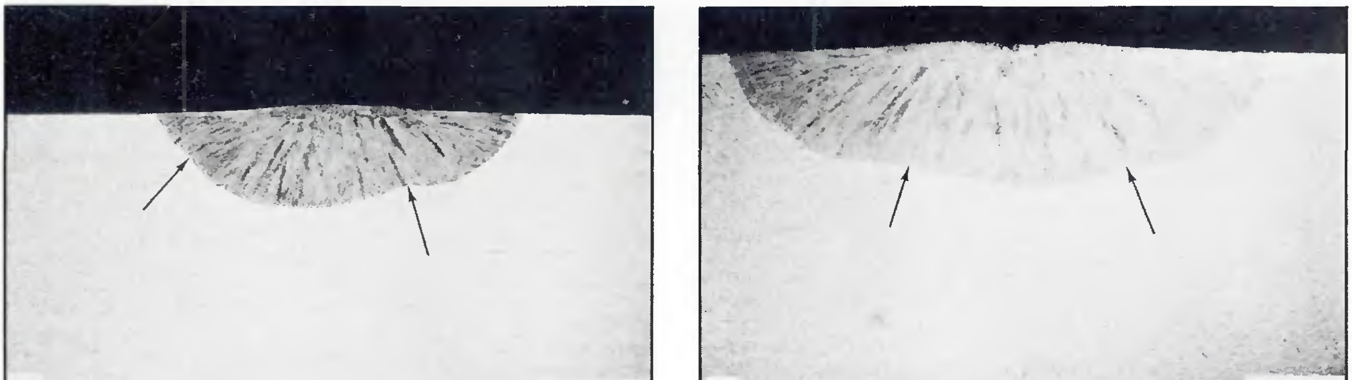

Fig. 1—Transverse macrograph of the GTA weld indicating the fusion zone shape and size (Heat A containing 90 ppm sulfur). A—After 2 s; B—after 5 s. Arrows indicate inflection in the fusion zone geometry.

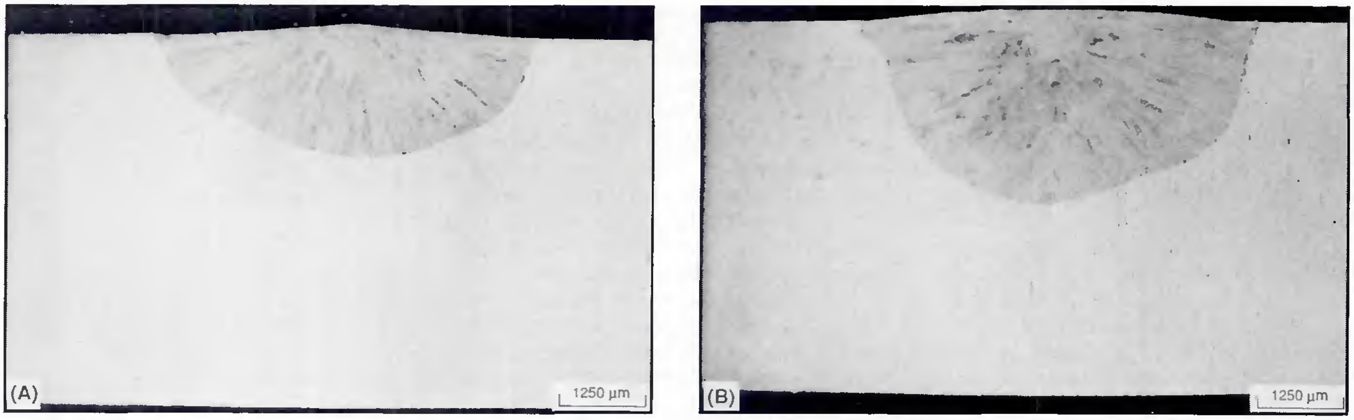

Fig. 2 — Transverse macrograph of the GTA weld indicating the fusion zone shape and size (Heat B containing 240 ppm sulfur). A — After 2 s; B — after 5 s.

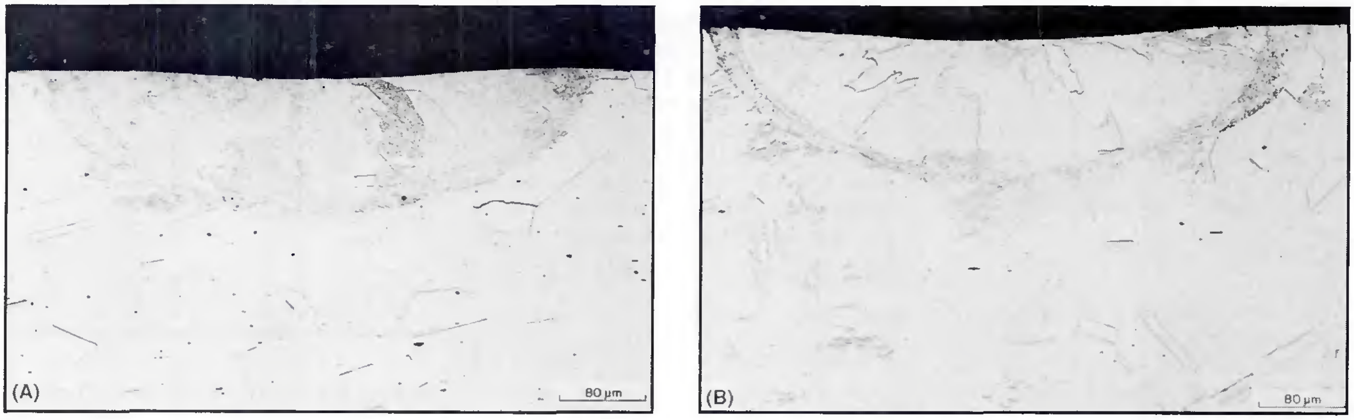

Fig. 3 — Transverse macrograph of the laser beam weld indicating the fusion zone shape and size (Heat A containing 90 ppm sulfur). A — After 2 s; B — after 5 s.

tains 240 ppm sulfur. This concentration of sulfur can be expected to be sufficient to alter the surface tension gradient and cause flow reversal (inward flow), even during stationary welding. Consequently, greater depth/width ratios can be expected for the welds deposited in this heat compared to the first heat of Type 304 steel. The transverse macrostructures of the stationary GTA welds after 2 and 5 s are presented in Fig. 2. Even though it is clear that after 2 s the depth of penetration is greater (Fig. 2A), it is not evident from the macrograph that there is a significant reversal of the flow field in the weld pool due to the high sulfur content. The weld pool shape is somewhat similar to that observed for the weld deposited in the lower sulfur heat (Heat A) (Fig. 1A). The macrograph shows a relatively shallow weld with a nearly comparable depth of penetration. The weld in Fig. 2A is narrower though, so that the depth/width ratio that is close to 0.3 is higher than the values obtained from Heat A. The computational modeling study predicted two convective loops at the surface: a large outward flow loop at the center of the pool and another small inward flow loop at the periphery of the pool. Therefore, there seems to be a qualitative agreement between theoretical predictions and experimental observations.

Figure 2B shows the transverse cross-section of the stationary GTA weld after 5 s. In this case, the shape of the weld is significantly different (Figs. 1–2), with a considerable increase in the penetration depth. Examination of the weld cross-section indicates the weld pool is almost cylindrical. A simple inward flow as reported by prior investigations cannot explain the observed shape of the pool, suggesting that the development of the weld pool was influenced by a complex flow field. The weld depth/width ratio in this case is 0.47. While the depth/width ratio increased with higher sulfur content, the observed values are considerably lower than those reported by previous experimental investigations (Refs. 1–5). Once again, this is likely due to the higher surface temperatures experienced by the stationary weld compared to the moving arc welds for which the earlier values were reported.

Laser Beam Welds

Stationary laser beam welds were made on Heat A inside a Plexiglas box under a controlled ultrahigh purity (UHP) argon atmosphere. The transverse sections of the welds after 2 and 5 s are presented in Figs. 3A and B, respectively. Examination of these figures shows that there are no significant changes in the size or shape between the two laser beam welds, suggesting that the weld has completely evolved in 2 s. This is consistent with the predictions of the computational model. It was shown (Ref. 6) that during laser beam welding, a quasisteady state is achieved rapidly and continued heating beyond 2 s did not result in any significant change in the size or shape of the weld.

The depth/width ratio for both laser beam welds was close to 0.28. Interestingly, this is very close to the depth/width ratio obtained for GTA welds. In contrast to the GTA welds, the fusion zone interface is a smooth curve that has no inflections. In addition, the weld pool is exactly symmetrical about the axis of the laser beam. The smooth and symmetrical fusion zone interface (no inflections) suggests that the driving forces for fluid flow in the weld pool, buoyancy and surface tension gradient, augment each other, resulting in a coherent flow field. This is in agreement with the theoretical predictions for laser beam welding presented in Part I.

Some of the laser beam welds were

made using a different source of argon shielding gas producing significantly different fusion zone structures and shapes from the results presented above. Typical transverse macrostructures of these welds after 2 and 5 s are presented in Figs. 4A and B, respectively. The results clearly show a significant difference in the penetration depth and width of the pool. The depth/width ratios for these welds are higher (close to 0.38). The macrographs show finely dispersed dark particles within the fusion zone (indicated by arrows A). Electron microprobe analysis identified these particles as chromium oxide inclusions, suggesting that the shielding gas was contaminated with oxygen (probably water).

Oxygen is surface active and can alter the surface tension gradient, thereby altering the flow field. If oxygen is readily available at the surface of the melt through the shielding gas, it is expected that there would be a sufficient concentration of oxygen at the melt surface to produce a positive $\frac{d\gamma}{dT}$ even at the high temperatures encountered during laser beam welding. The positive $\frac{d\gamma}{dT}$ at the weld pool surface can cause flow reversal resulting in the increased depth of penetration. Further, the simultaneous increase in the width of the pool suggests an increased melting efficiency, probably due to enhanced absorptivity. Sundell, *et al.* (Ref. 8), has reported in a previous study that oxygen added to the metal tends to increase both the depth and the width of the pool.

The weld macrostructure, shown in Figs. 4A and B, provides several clues about the fluid flow and heat transfer experienced by the weld during laser beam welding. Evaluation of the weld macrostructures reveals an oxide layer on the surface of the specimen toward the two edges of the fusion zone (indicated by arrows B). The presence of this oxide layer on the surface affects the surface tension gradient driven flow at these locations. In the center of the pool (at the surface), where the temperature is considerably greater than the melting point (2500 K) of Cr_2O_3, the oxide layer melts. Therefore, at these locations, the positive $\frac{d\gamma}{dT}$, due to the presence of oxygen, can overcome the buoyancy force and cause a downward flow at the center of the pool. Such a flow would transport hot liquid melt at the center of the weld pool from the surface to the bottom, causing increased depth of penetration. At the same time, toward the edges the buoyancy driven flow at the periphery of the weld transports hot liquid metal from the interior to the periphery enhancing the width of the pool. These opposing flows produce an inflection that was not observed in welds without the presence of oxygen.

Comparison of the weld macrostructures after 2 and 5 s shows negligible differences in the penetration depth and width of the pool. However, after 5 s of welding, the macrograph shows distinct changes in the fusion zone shape. The pronounced inflection in the fusion zone interface observed after 2 s of welding is not as apparent after 5 s. The most unusual feature of the weld is the continuous oxide layer within the fusion zone. Theoretical analysis of the heat flow in the weld pool indicates that this continuous layer of oxide roughly represents the 2500 K isotherm in the weld pool, which is the melting point of Cr_2O_3. This is supported by the actual experimental observations. The weld macrostructure clearly shows that this oxide layer extends to the surface of the weld pool and joins the extremity of the oxide layer at the surface of the weld pool established after only 2 s. This continuous layer divides the molten pool into two sections. The top section (above the oxide layer) has a free surface, and therefore, the surface tension gradient is the predominant driving force for fluid flow in this region. In the bottom section (below the oxide layer), since liquid metal in this section is isolated from the free surface effects, the flow is driven predominantly by buoyancy together with the effects of momentum transport at the interface of the two region through viscous effects. The oxide layer can significantly influence the fluid flow in the weld pool, thereby influencing the fusion zone shape.

Comparison with Theoretical Predictions

A computational model based on the work of Paul and DebRoy (Ref. 9) was used to calculate the weld size and shape. Details of the model and the results are presented in Part I. The weld macrostructures presented in the previous section show good agreement with the predictions of the model. The overall shape, and in some instances particular features of the weld, agreed well with the calculated flow and temperature field in the weld pool. Experimental measurements of velocities and temperature profiles are difficult due to the small size of the weld pool and the presence of the arc. Hence, validation of the calculated velocities and temperatures are extremely difficult. However, the cumulative effect of the flow field and the temperature field on the weld geometry can be readily obtained by light microscopy of the transverse section of the weld. In this section, the predictions of the computational model are verified by comparing in detail the calculated and observed fusion zone shape and size. Further, the results of the theoretical analysis are used to interpret some of the experimental observations.

The calculated temperature field and flow field are presented concurrently with the weld macrostructure in order to facilitate comparison between the two. The experimentally observed and predicted results after 2 and 5 s of GTA welding (Heat A) are presented in Figs. 5 and 6, respectively. The results, after both 2 and 5

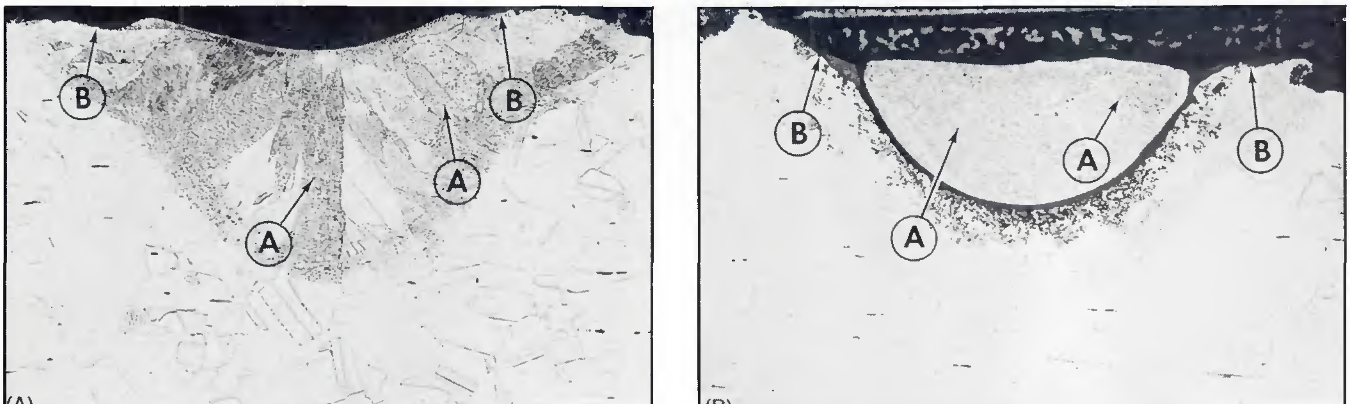

Fig. 4 — Transverse macrograph of the laser beam weld indicating the fusion zone shape and size (Heat A containing 90 ppm sulfur; shielding gas contaminated with oxygen). A — After 2 s; B — after 5 s. Arrows A indicate Cr_2O_3 particles within the fusion zone and B indicate the Cr_2O_3 layer near the edge of the pool.

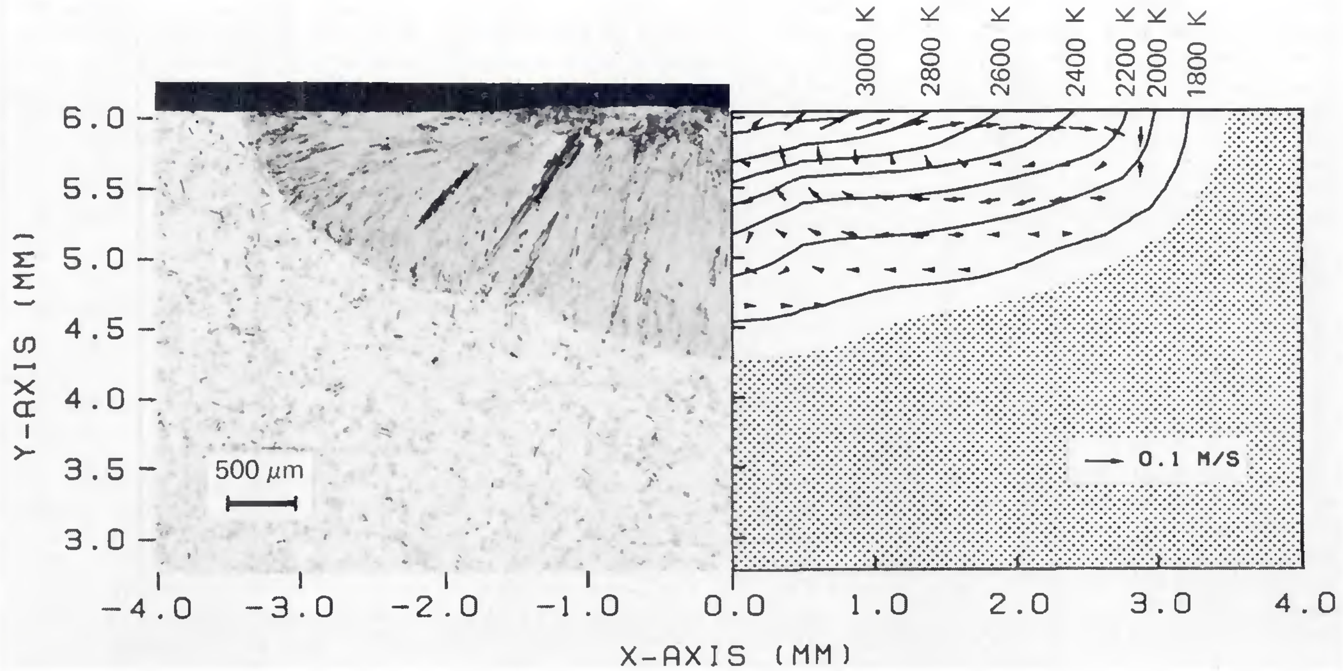

Fig. 5 — Comparison of the calculated and experimentally observed GTA weld fusion zone after 2 s (Heat A containing 90 ppm sulfur).

s, show excellent agreement between the predicted and experimentally observed fusion zone shape and size. Further, the predicted features of the fusion zone interface agreed very well with the experimental observations. The fluid flow pattern evident in the calculated pool profile provides insight into the evolution of the weld pool due to the convective heat transfer. Even though there exist opposing surface tension gradient effects on the weld pool surface (Ref. 6), the negative $\frac{d\gamma}{dT}$ over much of the weld pool surface prevails and controls the surface flows. The calculated flow field is radially outward, transporting heat from the center to the periphery of the pool. In the interior of the weld pool, the electromagnetic force prevails, causing a minimal flow in the radially inward direction. The observed inflection in the fusion zone interface is due to this minimal flow causing increased local penetration. This relatively weak influence of the electromagnetic force is consistent with previous experimental investigations, which suggested that the welding current has to exceed 150 A in order for the electromagnetic force to have any significant impact on the fluid flow and consequently on the weld pool shape and size.

The calculated temperature fields are overlaid on the predicted flow field in order to show the influence of convection on the temperature distribution in the weld pool. Due to the radially outward flow, the heat from the welding arc is transported from the center to the periphery of the weld pool causing the isotherms to be shallow. Within the weld pool, the effect of the surface flow on the temperature fields diminishes with distance from the weld pool surface. This is particularly evident at the center of the pool where the radially inward flow due to the electromagnetic force transports relatively hot liquid from the periphery to the interior, causing the isotherms to be deeper at these locations.

The experimentally observed and theoretically predicted results obtained for GTA welding of Heat B are presented concurrently in Figs. 7 and 8. Comparison of the calculated and experimentally observed fusion zone geometry shows reasonable agreement, after 2 s. The calcu-

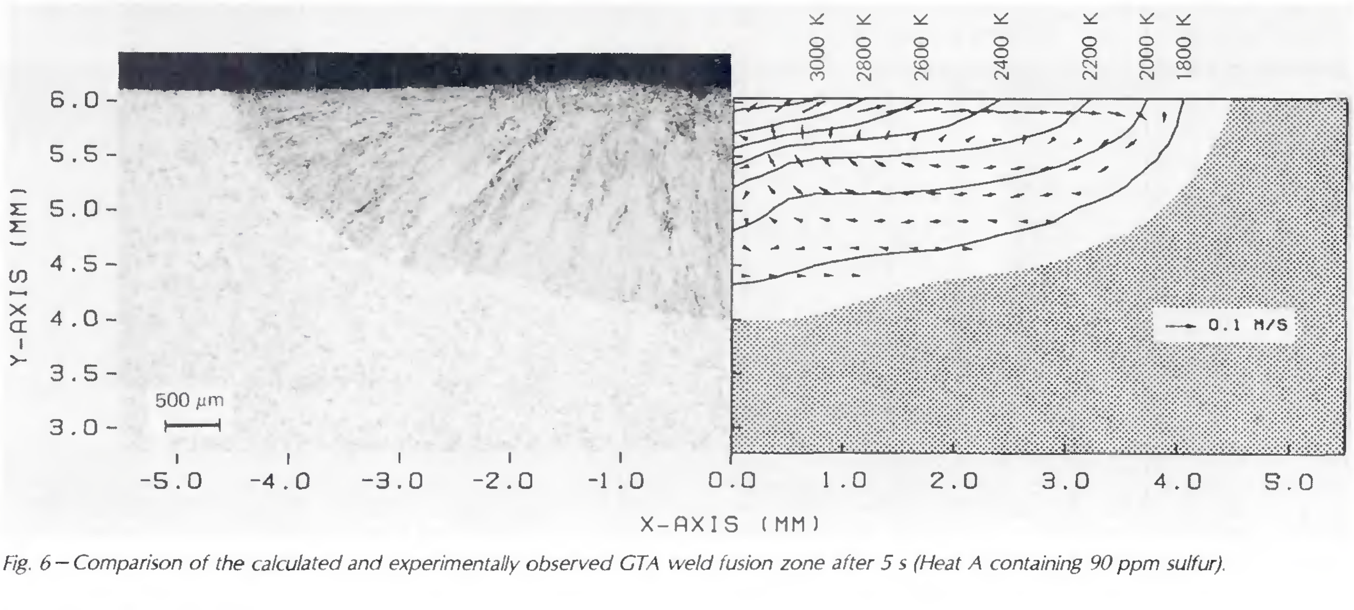

Fig. 6 — Comparison of the calculated and experimentally observed GTA weld fusion zone after 5 s (Heat A containing 90 ppm sulfur).

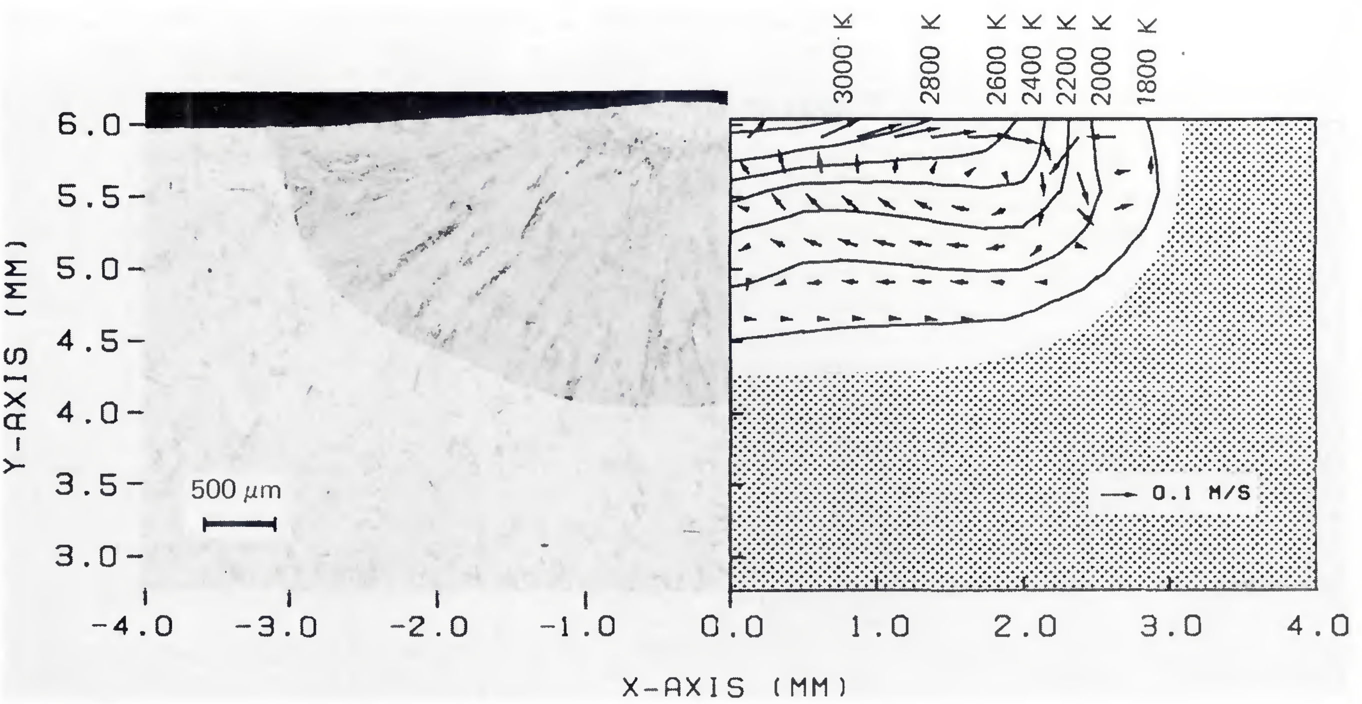

Fig. 7 — Comparison of the calculated and experimentally observed GTA weld fusion zone after 2 s (Heat B containing 240 ppm sulfur).

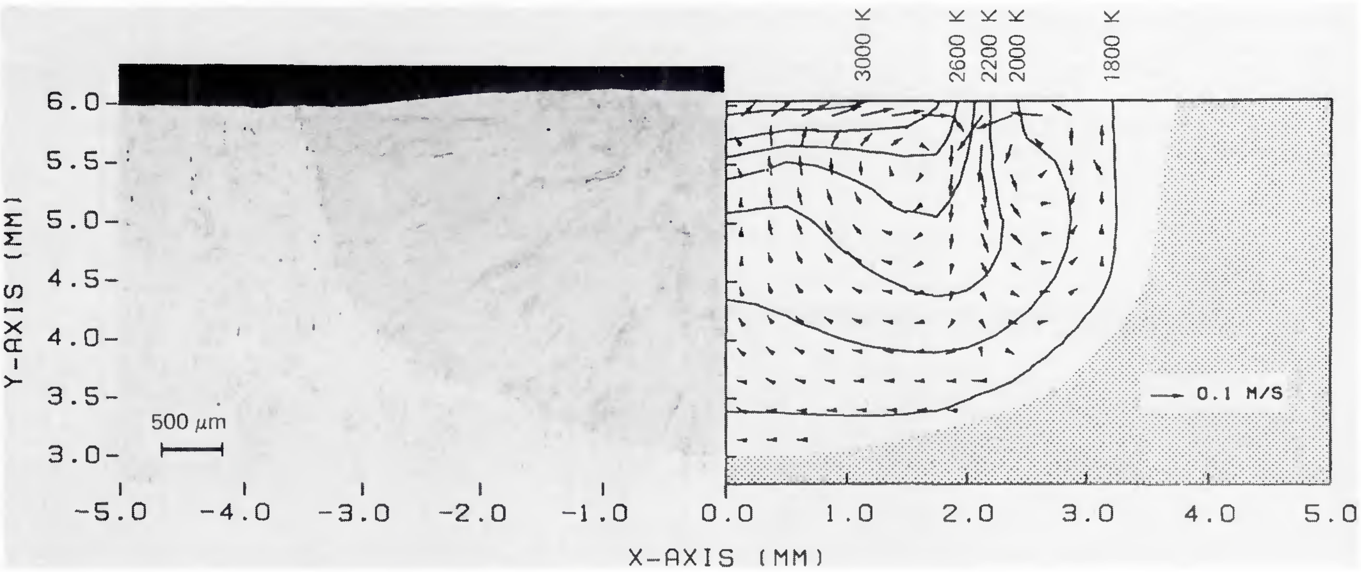

Fig. 8 — Comparison of the calculated and experimentally observed GTA weld fusion zone after 5 s (Heat B containing 240 ppm sulfur).

lated size of the weld (penetration depth) is smaller than the experimentally observed weld. The predicted flow field has a predominant outward flow over much of the weld pool and an inward flow near the cooler periphery of the weld pool. Therefore, in the presence of the higher sulfur content, the heat from the arc is not transported to the periphery as efficiently as in the previous case, resulting in a decreased width of the weld. The temperature distribution in the weld pool shows that the region (T < 2500 K) where a positive $\frac{d\gamma}{dT}$ can exist at the surface is very small, particularly in the initial stages of the weld development. In order for the model to predict the complete effects of this inward flow, the enmeshment must possess an extremely fine resolution during the initial stages, which would require excessive computer time. The results indicate that as the pool grows with continued heating beyond 2 s, the problem is less severe due to the increased resolution (increased size of the weld pool) of the enmeshment.

Figure 8 shows the experimental and calculated results after 5 s. Comparison of the predicted and experimentally observed fusion zone once again indicates excellent agreement. The results, as expected, indicate the significant effect of a surface active element (sulfur) on the fluid flow pattern. Instead of the simple inward flow as suggested by earlier investigations (Ref. 8–13), the results indicate a complex bifurcated flow pattern with radially outward and inward loops on the surface of the weld pool. With continued heating beyond 2 s, the positive $\frac{d\gamma}{dT}$ at the periphery controls the local flow field, causing a radially inward flow near the solid-liquid interface. The radially outward loop near the centerline of the weld transports heat from the center of the pool to the periphery. However, in this case, the relatively hot liquid metal is met by a radially inward flow that is transporting heat from the sides to the interior. The ensuing convective heat transfer produces an almost cylindrical weld pool with increased depth of penetration at the periphery instead of at the center of the weld pool. The results also show the significant influence the fluid flow has on the temperature distribution in the weld pool.

It has already been mentioned (Ref. 6) that previous attempts to quantitatively study the effect of surface active elements on weld pool fluid flow considered a specified constant positive $\frac{d\gamma}{dT}$ (Refs. 8–13). This assumption, due to the lack of adequate surface tension data, cannot be justified based on the physical phenomena governing the process and may lead to erroneous conclusions. In order to illustrate the importance of calculating $\frac{d\gamma}{dT}$ as a function of temperature and activity, the fluid flow and the consequent weld pool shape and size were calculated assuming a constant positive $\frac{d\gamma}{dT}$ of 0.15×10^{-03} N/m-K. The computed flow field and temperature field for GTA welding, after 2 s, are presented in Fig. 9. The results show an inward flow pattern causing an unrealistically high depth of penetration. The results clearly show the considerable difference in the calculated shape and size of the pool in relation to the experimental observations.

The experimentally observed and predicted results for laser beam welds after 2 s are presented concurrently in Fig. 10. Comparison of the calculated and experimentally observed fusion zone shape and size shows excellent agreement again. The results show a single vortex during laser beam welding. Since $\frac{d\gamma}{dT}$ is largely negative, the resulting flow is radially outward at the weld pool surface. This flow is augmented by the buoyancy driven flows in the interior of the pool. The radially outward flow produces a relatively shallow weld pool by transferring the heat from the center to the periphery.

Microstructure

Following conventional GTA welding, the weld metal contained a duplex austenite + ferrite ($\gamma + \delta$) microstructure. There were no significant variations in the solidification structure between the two heats of stainless steel considered in this investigation. Figure 11 shows a typical microstructure of the GTA welds indicating the duplex structure. With increasing weld duration, light microscopy indicated a relatively coarse solidification substructure with a widely spaced ferrite network. This is attributed to the reduction in the cooling rates and the solidification rates with increased weld duration. Laser beam welds, on the other hand, produced fully austenitic microstructures for all the welding conditions. Figure 12 shows a typical microstructure of the laser beam welds indicating a completely austenitic structure. Previous work by the authors has shown that solidification of the weld metal at high cooling rates ($\approx 10^5$ $K \cdot s^{-1}$) can cause significant microstructural modifications compared to microstructures after conventional GTA welding (Ref. 14). The observed fully austenitic structure at these high cooling rates is attributed to the change in mode of solidification from primary ferritic to primary austenitic (Ref. 15).

Significant modifications were observed in the solidification structure of the laser welds made in the presence of oxygen. For example, Fig. 13 shows the microstructure of the laser beam weld after 2 s. The photomicrograph shows a fully austenitic structure with a fine dispersion of dark particles later identified as fine inclusions of Cr_2O_3. Interdendritic regions appear dark due to segregation of these particles to the interdendritic liquid. During welding, chromium in the liquid melt at the weld pool surface oxidizes readily due to availability of oxygen in the shielding gas. The chromium oxide thus formed remains molten at locations on the weld pool surface where the temperature is above 2500 K (the melting temperature of Cr_2O_3). Relatively large flows at the sur-

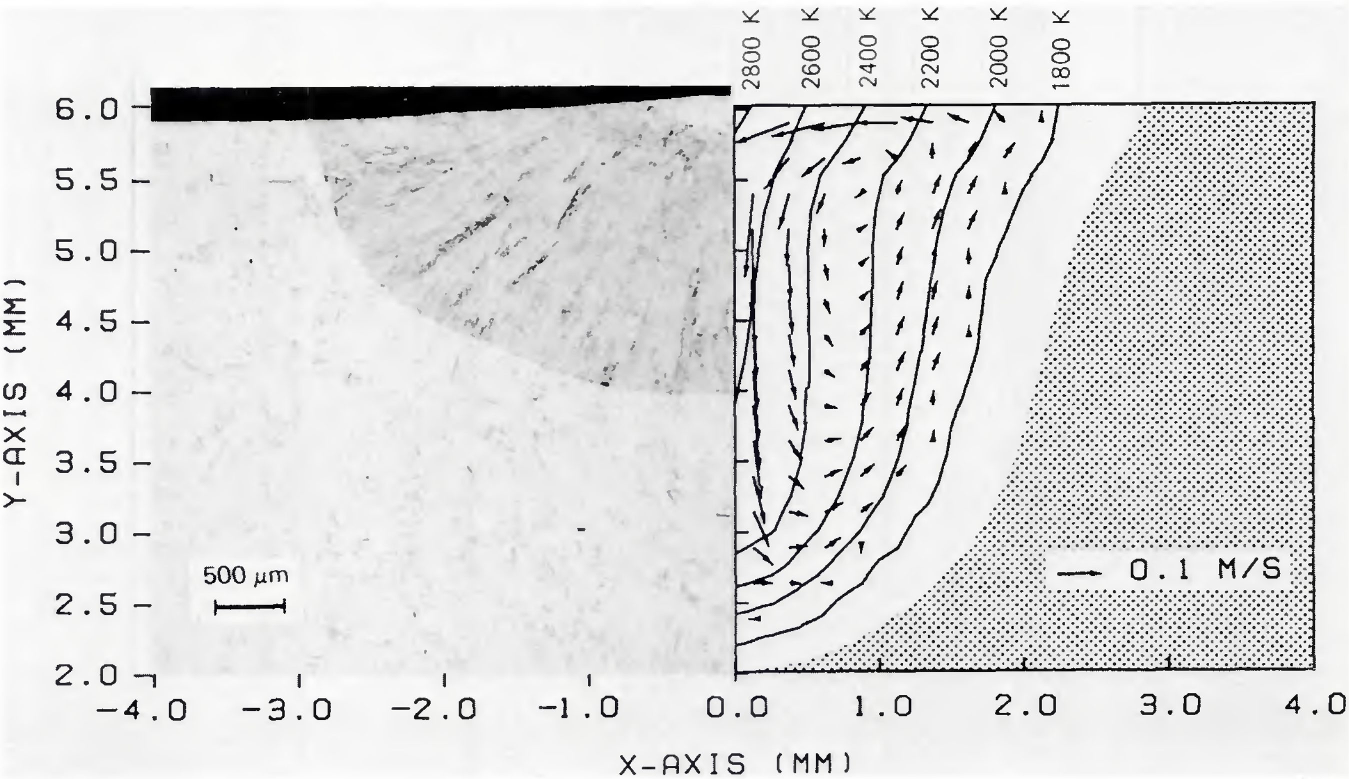

Fig. 9—Comparison of the calculated (for a constant $\frac{d\gamma}{dT}$ of 0.15×10^{-3} N/m-K) and experimentally observed GTA weld fusion zone after 2 s (Heat B containing 240 ppm sulfur).

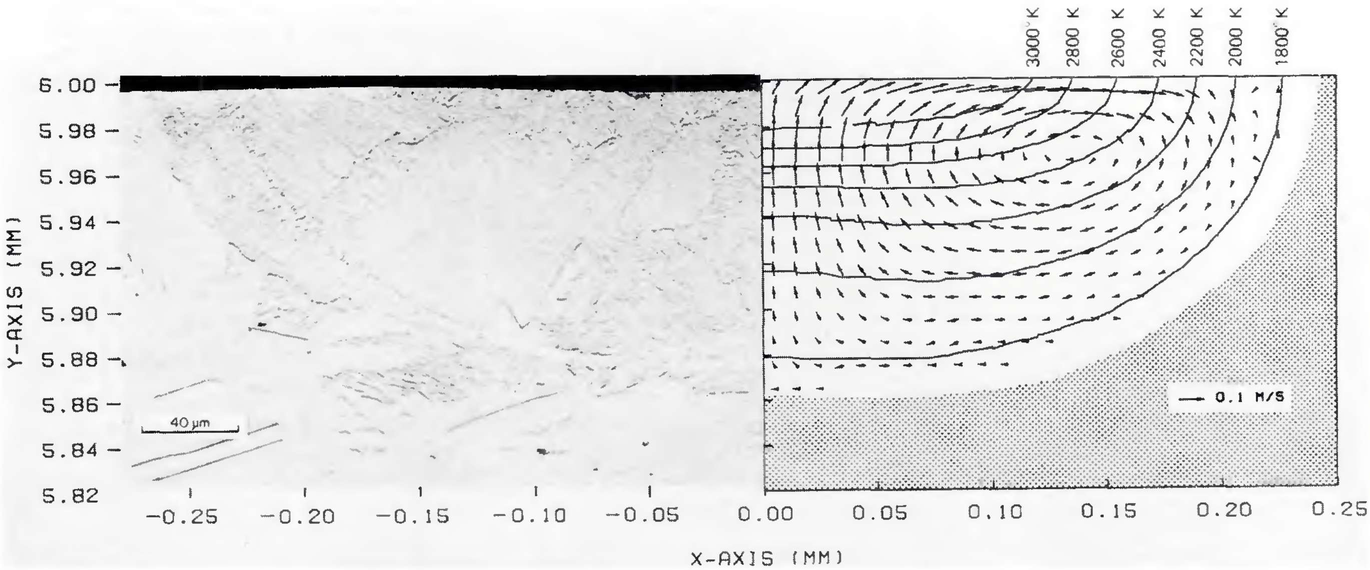

Fig. 10—Comparison of the calculated and experimentally observed laser beam weld fusion zone after 2 s (Heat A containing 90 ppm sulfur).

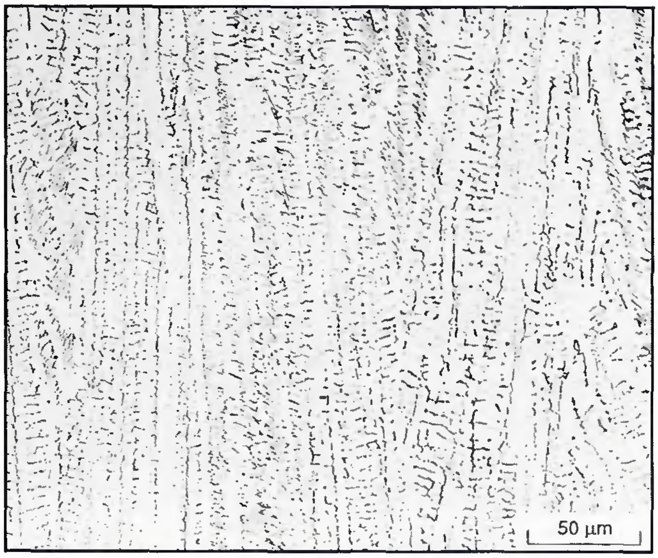

Fig. 11—Microstructure of Type 304 (Heat A) GTA weld after 2 s of welding.

Fig. 12—Microstructure of Type 304 (Heat A) laser beam weld after 2 s of welding.

Fig. 13—Microstructure of Type 304 (Heat A) laser beam weld after 2 s of welding (shielding gas contaminated with oxygen).

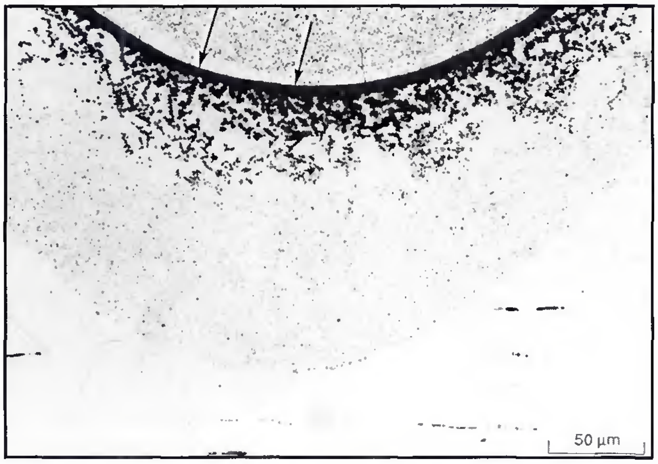

Fig. 14—Microstructure of Type 304 (Heat A) laser beam weld after 5 s of welding (shielding gas contaminated with oxygen). Arrows indicate the continuous Cr_2O_3 layer within the fusion zone.

RESEARCH/DEVELOPMENT/RESEARCH/DEVELOPMENT/RESEARCH/DEVELOPMENT/RESEARCH/DEVELOPMENT/RESEARCH/DEVELOPMENT

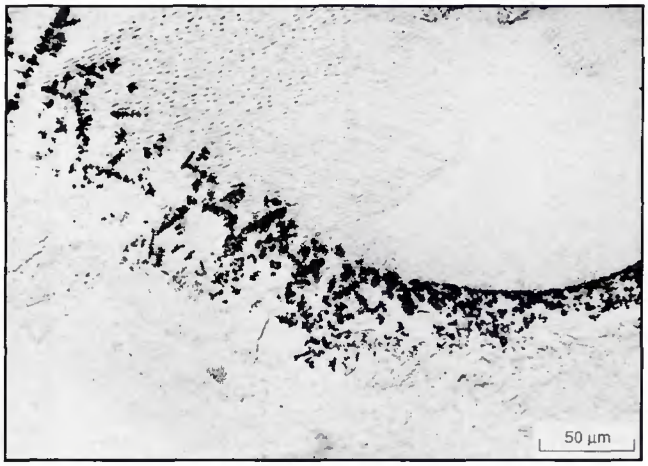

Fig. 15 — Microstructure of Type 304 (Heat A) laser beam weld after 5 s, showing the initial stages of the formation of the continuous oxide layer (shielding gas contaminated with oxygen).

face ($\approx$ 0.4 m/s) cause the molten Cr_2O_3 to break up, which then gets trapped in the recirculating flow and is transported with the liquid metal. Since molten Cr_2O_3 is immiscible in the liquid metal, it forms inclusions upon solidification.

Figure 14 shows the microstructure of the laser beam weld after 5 s. The microstructure shows, as expected, finely dispersed Cr_2O_3 inclusions in the fusion zone. The most unusual microstructural feature is the observation of the continuous band of oxide layer embedded within the fusion zone (indicated by arrows). With continued heating, the amount of chromium oxide in the recirculating melt continues to increase. Consequently, these oxide particles can merge to form larger particles. As the Cr_2O_3 particles are transported to the bottom half of the pool, where the temperature of the liquid melt is below 2500 K (melting point of Cr_2O_3), they would solidify as indicated by the dendritic structure of the oxide particles. Since the oxide particles are lighter than the liquid melt, the larger particles can escape the recirculating flow field and would tend to rise to the top. It is likely that these particles may have fused together at temperatures near the melting point of chromium oxide to form the observed continuous layer. The test welds were repeated to substantiate the formation of this oxide layer. In one instance, the fusion zone microstructure revealed the early stages of the formation of this continuous oxide layer — Fig. 15. The photomicrograph shows individual dendrites of chromium oxide merging together to form the continuous layer. The remainder of the micrograph shows a completely austenitic structure.

Summary and Conclusions

The predictions of the computational model were verified by comparing the numerically predicted and experimentally observed fusion zone size and shape. The predicted weld pool geometry (size and shape) agreed very well with the experimental observations for both GTA and laser beam welds. The results confirmed the significant influence of surface active elements such as sulfur and oxygen on the fluid flow and the convective heat transfer. The importance of considering a temperature dependent $\frac{d\gamma}{dT}$ was also clearly shown. The computer simulation considered the effect of sulfur on the development of the weld pool by calculating $\frac{d\gamma}{dT}$ as a function of the concentration of the surface active elements and the temperature. It has been shown that the weld penetration and the aspect ratio are not determined solely on the basis of the level of the surface active element in the base metal but rather by a combination of the level of surface active elements and the temperature distribution.

The results of the experimental investigation show relatively shallow welds (low depth/width ratios) for both welding processes. The depth/width ratio for both GTA and laser beam welds were on the order of 0.28. Increasing the sulfur content of the Type 304 alloy increased the weld penetration, as expected, during GTA welding. The observed increase in penetration was considerably less than the values reported by earlier investigations. This is attributed to the higher surface temperatures during stationary welding that can cause $\frac{d\gamma}{dT}$ to change from a positive value to a negative value.

The effect of oxygen on weld penetration during laser beam welding was to significantly increase the weld penetration and width of the pool. Contrary to previous studies, the results of the present investigation for stationary laser beam welds show a significant increase in the depth/width ratio. Microstructural evaluation of the fusion zone showed a fine dispersion of chromium oxide inclusions. The most unusual feature of the fusion zone structure is the experimentally observed continuous oxide layer within the fusion zone.

The observed microstructures were sensitive to the cooling rates. Following conventional welding, the weld metal solidified with a duplex $\gamma + \delta$ structure. Increasing the weld duration (decreasing the cooling rate) resulted in a coarser solidification substructure with a widely spaced ferrite network. Also, at the top center of the pool where the calculated cooling rates were relatively low, light microscopy indicated a relatively coarser solidification structure. The rapid solidification of the material (cooling rates of the order of 10^5 $K \cdot s^{-1}$) after laser beam welding resulted in a fully austenitic microstructure with a fine solidification substructure.

Acknowledgments

The authors would like to thank S. K. Iskander and M. Maguire for reviewing the manuscript, R. W. Reed and M. M. Collur for welding, and G. C. Marsh for metallography. The research was sponsored by the Div. of Materials Sciences, U. S. Dept. of Energy, under contract DE-AC05-84OR21400 with Martin Marietta Energy Systems, Inc.

References

1. Heiple, C. R., and Roper, J. R. 1982. Mechanism for minor element effect on GTA fusion zone geometry. *Welding Journal* 61 (4):97-s.

2. Heiple, C. R., Roper, J. R., Stagner, R. T., and Alden, J. J. 1983. Surface active element effects on the shape of GTA, laser and electron beam welds. *Welding Journal* 62(3):72-s.

3. Heiple, C. R., and Roper, J. R. 1981. Effect of selenium on GTAW fusion zone geometry. *Welding Journal* 60(8):143-s.

4. Heiple, C. R., and Burgardt, P. 1985. Effects of SO_2 shielding gas additions on GTA weld shape. *Welding Journal* 64(6):159-s.

5. Heiple, C. R., and Roper, J. R. 1981. Effects of minor elements on GTAW fusion zone shape. *Trends in Welding in the United States*, Ed. S. A. David, ASM International, Materials Park, Ohio. p. 489.

6. Zacharia, T., David, S. A., Vitek, J. M., and DebRoy, T. 1989. Weld pool development during GTA and laser beam welding of Type 304 stainless steel. Part I — Theoretical analysis. *Welding Journal*. 68(12).

7. Sahoo, P., DebRoy, T., and McNallan, M. J. 1988. Surface tension of binary metal-surface active solute systems under conditions relevent to welding metallurgy. *Metall. Trans.* Vol. 19B, p. 483.

8. Sundell, R. E., Correa, S. M., Harris, L. P., Solomon, H. D., Wojcik, L. A., Savage, W. F.,

Walsh, D. W., and Lo, G-D. 1986. Minor element effects on gas tungsten arc weld penetration. GE Report No. 86SRD013.

9. Paul, A., and DebRoy, T. 1988. Free surface flow and heat transfer in conduction mode laser welding. *Metallurgical Transactions.* 19B, pp. 851-858.

10. Oreper, G. M., and Szekely, J. 1984. Heat and fluid flow phenomena in weld pools. *Journal of Fluid Mechanics.* Vol. 147, p. 53.

11. Kou, S., and Wang, Y. H. 1986. Weld pool convection and its effect. *Welding Journal* 65(3):63-s.

12. Zacharia, T., Eraslan, A. H., and Aidun, D. K. 1988. Modeling of non-autogenous welding. *Welding Journal* 67(1):18-s.

13. Zacharia, T., Eraslan, A. H., and Aidun, D. K. 1988. Modeling of autogenous welding. *Welding Journal* 67(3):53-s.

14. David, S. A., Vitek, J. M., and Hebble, T. L. 1987. Effect of rapid solidification on stainless steel weld metal microstructures and its implications on the Schaeffler diagram. *Welding Journal* 66(10):289-s.

15. Zacharia T., David, S. A., Vitek, J. M., and DebRoy, T. 1989. Heat transfer during Nd:YAG pulsed laser welding and its effect on solidification structure of austenitic stainless steels. *Metallurgical Transactions* 20A, pp. 1125-1138.

WRC Bulletin 331
February 1988

This Bulletin contains two reports prepared by the Japan Pressure Vessel Research Council (JPVRC) Subcommittee on Pressure Vessel Steels. The reports are involved with the variation in toughness data for weldments in pressure vessel steel structures.

Metallurgical Investigation on the Scatter of Toughness in the Weldment of Pressure Vessel Steels—Part I: Current Cooperative Research

This report covers the background of current cooperative research from 1973 to the present, covering 137 references on toughness and toughness testing of weldments.

Metallurgical Investigation on the Scatter of Toughness in the Weldment of Pressure Vessel Steels—Part II: Cooperative Research

The objective of this report was to investigate the variation in toughness of multipass weldments in a welded joint.

Publication of these reports was sponsored by the Subcommittee on Thermal and Mechanical Effects on Materials of the Welding Research Council. The price of WRC Bulletin 331 is $28.00 per copy, plus $5.00 for postage and handling. Orders should be sent with payment to the Welding Research Council, 345 E. 47th St., Suite 1301, New York, NY 10017.

WRC Bulletin 332
April 1988

This Bulletin contains two reports that characterize the mechanical properties of two different structural shapes of constructional steels used in the pressure vessel industry.

(1) Characteristics of Heavyweight Wide-Flange Structural Shapes
By J. M. Barsom and B. G. Reisdorf

This report presents information concerning the chemical, microstructural and mechanical (including fracture toughness) properties for heavyweight wide-flange structural shapes of A36, A572 Grade 50 and A588 Grade A steels.

(2) Data Survey on Mechanical Property Characterization of A588 Steel Plates and Weldments
By A. W. Pense

This survey report summarizes, for the most part, unpublished data on the strength toughness and weldability of A588 Grade A and Grade B steels as influenced by heat treatment and processing.

Publication of this Bulletin was sponsored by the Subcommittee on Thermal and Mechanical Effects on Materials of the Pressure Vessel Research Committee of the Welding Research Council. The price of WRC Bulletin 332 is $20.00 per copy, plus $5.00 for postage and handling. Orders should be sent with payment to the Welding Research Council, Suite 1301, 345 E. 47th St., New York, NY 10017.

WRC Bulletin 342
April 1989

Stainless Steel Weld Metal: Prediction of Ferrite Content
By C. N. McCowan, T. A. Siewert and D. L. Olson

A new diagram to predict the ferrite number (FN) in stainless steel welds is proposed in this Bulletin. The diagram has a range from 0 to 100 FN and more accurately predicts the ferrite content for welds having a FN less than 18. The database contains over 950 welds and is included as an appendix to the report.

Publication of this report was sponsored by the Subcommittee on Welding Stainless Steel of the High Alloys Committee of the Welding Research Council. The price of WRC Bulletin 342 is $20.00 per copy, plus $5.00 for postage and handling. Orders should be sent with payment to the Welding Research Council, Room 1301, 345 E. 47th St., New York, NY 10017.